Void-Volume-Based Stem Geometric Modeling and Branch-Knot Localization in Terrestrial Laser Scanning Data

Aravind Harikumar, *Member, IEEE*, Xinlian Liang, *Senior Member, IEEE*, Francesca Bovolo, *Senior Member, IEEE*, and Lorenzo Bruzzone, *Fellow, IEEE*

***Abstract*—A comprehensive 3-D structural mapping of stem is essential for an accurate 3-D crown modeling and tree parameter estimation. Terrestrial laser scanning (TLS) is an effective technology for a comprehensive collection of individual tree level data, compared to destructive and costly field measurements. The performance of 3-D stem modeling techniques is adversely affected by laser shadowing and point-density variations in TLS data. In addition, most of the state-of-the-art techniques perform stem modeling using regular geometric shapes, such as circle, ellipse, and cylinder, which cannot accurately capture the complex 3-D stem geometric shapes. This results in stem modeling errors. In this article, we propose a 3-D stem modeling approach for both single- and multiscan TLS data that: 1) does not make any prior assumption on the stem geometry and 2) is minimally affected by undesirable stem shadowing and point-density variations. The proposed approach accurately models 3-D stem and localizes branch-knots for both coniferous and deciduous trees by mapping the void volume formed within the stem due to the opaqueness of tree stem to laser. The modeling performance was evaluated on both single- and multiscan data obtained for pine, spruce, and birch species. The low estimation errors associated with the stem diameter at breast height and branch-knot location, compared to the reference methods, prove the ability of the proposed method to both accurately model 3-D stem and localize branch-knots.**

***Index Terms*—Branch-knot localization, diameter at breast height (DBH), remote sensing, stem detection, stem modeling, terrestrial laser scanning (TLS).**

I. Introduction

ACCURATE 3-D crown structural characterization is central to the next-generation individual tree-level forest inventory and precision forest management [1]. Attributes derived from major crown components, including the stem, branches, and leaves, are used to build detailed tree models that provide accurate estimates of biophysical parameters [2], [3]. The usability of a tree model is determined by the level of details (LoD) that it contains. A simple model at the first level of description (LoD-1) defines a tree using only the stem diameter at breast height (DBH) and the tree height [4]. Thus, it is beneficial for biomass studies. More complex models, such as LoD-2, LoD-3, LoD-4, and LoD-5, provide increasingly more crown details about branches and leaves and, hence, are useful in accurate forest parameter estimation and environmental modeling [4]. An accurate structural characterization of the 3-D stem is critical to all the models and benefits from improvement in the localization of branch-knots.

Terrestrial laser scanning (TLS) allows us to perform a comprehensive structural mapping of tree crown components, such as stem, branches, and leaves. The TLS full-view (360° $\otimes$ 310°) data collection in forests can be performed in single- and multiscan acquisition modes. The single-scan mode has simple data acquisition setting, where the laser scanner is usually placed proximal to the plot center. In case of stem with a regular geometry, this mode of acquisition puts one-half of the stem within the laser shadowed zone. Multiscan TLS acquisition captures and coregisters data collected from multiple TLS single scans performed at widely separated locations within the plot and, hence, has the potential to capture much more comprehensive geometric details of stem [4]. The dense and accurate TLS point measurements from TLS scanning allow the accurate estimation of stem parameters, including DBH [5] and stem curve [6], which are important biophysical variables required in most forest-based analyses or studies [4], [7]. However, both single- and multiscan data of tree crown are affected by laser occlusion caused by its own branches, foliage, and even neighboring tree crowns [8]. In this context, a fully automatic and accurate 3-D stem modeling technique robust to noise and occlusion effects in TLS forest data is essential to perform time-critical forest inventorying, by minimizing manual/field mapping.

Considering the general circular shape of stem cross section, a common approach to model them is by fitting regular geometric shapes, such as circles [9] or cylinders [2]. However, trees often do not grow straight (i.e., resulting in curved stem), and hence, geometric shape fitting is performed on local stem slices in the vertical direction (i.e., along the Z-axis) and is finally merged to generate a complete stem model. By fitting circles on ground

Manuscript received February 8, 2022; revised March 14, 2022; accepted March 24, 2022. Date of publication March 30, 2022; date of current version April 28, 2022. *(Corresponding author: Aravind Harikumar.)*

Aravind Harikumar is with the University of Toronto Mississauga, Mississauga, ON L5L 1C6, Canada (e-mail: aravindhari1@gmail.com).

Xinlian Liang is with the Wuhan University, China (e-mail: xinlian.liang@whu.edu.cn).

Francesca Bovolo is with the Fondazione Bruno Kessler, 38122 Trento, Italy (e-mail: bovolo@fbk.eu).

Lorenzo Bruzzone is with the University of Trento, 38122 Trento, Italy (e-mail: lorenzo.bruzzone@ing.unitn.it).

Digital Object Identifier 10.1109/JSTARS.2022.3163404

(i.e., XY plane) projected TLS data of vertical stem sections, the so-called circular-shape-fitting-based stem modeling is a widely accepted technique to estimate stem center and diameter [10], [11]. Using a more realistic assumption of elliptical stem cross sections, Harikumar *et al.* [12] approximated the 3-D stem structure by using a moving-average stem sectioning strategy and obtained improved results for pine, spruce, and birch species. Alternatively, stem modeling using cylindrical shape is achieved by dividing tree point cloud into multiple vertical slices and by fitting TLS data in each slice with a cylinder that is parameterized by its own orientation and radius [13]. Although geometric shape fitting can be reliably performed using least squares in the presence of minimum noise [14], [15], robust circle [16], cylinder fitting [17], and random sample consensus (RANSAC) [11], [18] based techniques are preferred to get improved fit in noisy environments such as complex forests with overlapping crowns and undergrowth. Liang *et al.* [8] delineated stem sections based on the flatness and normal-vector directions of the local cloud segments, in addition to considering the overall geometric shape of the entire TLS point cloud. In a recently developed approach, Holmgren *et al.* [19] performed stem modeling by progressively merging/removing stem sections, to the seed section identified using circle fitting. However, the method often overestimates the stem diameter due to inclusion of branch sections as part of the stem. As evident from the literature, most 3-D stem modeling methods [8], [20] rely on a sectionwise analysis along the height profile. However, the performance of most stem modeling methods is largely affected by issues such as: 1) partial stem occlusion resulting from laser beam occlusions by opaque branches and foliage and 2) the decrease in point density from the bottom to the top of a tree due to the increase in the distance between the target and the sensor [21]. These issues whatsoever exist in the TLS point cloud regardless of careful planning. The stem occlusion effect is usually extreme in single-scan data and is minimized by performing multiple scans from multiple locations within the site [22]. The crescent moon method by Király and Brolly [23] tried to minimize the effect of occlusion in stem models by specifically modeling the visible section of the partially occluded stem. However, the methods show large bias in the presence of noisy points (i.e., point corresponding to branches and foliage). Methods to directly estimate model stem from the TLS point cloud using techniques, such as 3-D clustering [23], skeletonization [24], and Hough transform [9], also exist in the literature. However, the undesirable effects of shadowing and point-density variation degrade modeling performance. Considering the fact that parametric-shape-fitting-based stem modeling compromises on stem detail, complementary fitting procedures that further refine the models by slice analysis were also proposed [22]. A hybrid approach that incorporates field-collected reference data to improve stem modeling allows us to improve stem modeling at the increased cost of reference data collection [25]. Yrttimaa *et al.* [26] proposed a multisensor approach to improve stem modeling by augmenting TLS data with photogrammetric point cloud generated from drone-based multispectral sensors, at increased data acquisition cost. For cases where large training data are available, a deep learning approach for semantically segmenting high-resolution forest point also shows considerable potential in accurate 3-D stem modeling [27].

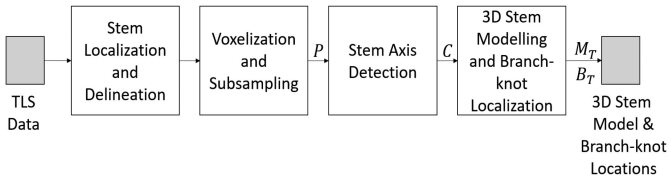

Fig. 1. Block scheme of the proposed 3-D stem modeling and branch-knot localization method.

The first-order branches meet the 3-D stem at location referred to as the branch-knots and are used to derive information about species and quality of wood [28]. In addition, the accurate localization of branch-knots benefits accurate tree modeling (e.g., all the models more detailed than the LoD1). Gorte and Pfeifer [24] performed voxel-level skeletonization of TLS data, and delineated stem, and identified both first-order branches and branch-knots by exploiting the differences in internode neighborhood relationship. Based on the assumption that branch locations around the stem are associated with a high density of points away from the stem surface, Pyörälä *et al.* [29] detected branch-knot by associating the peaks in point-density and mean point-distance distribution along the radial direction (from stem center) with the presence of branches. In another work, Pyörälä *et al.* [30] detected branch-knot locations (BKLs) in vertical segment using the Gaussian smoothed histogram of branch point count around the stem, using the continuous wavelet transform peak detection method. However, both the approaches rely on a sectionwise analysis of branches. Hence, in situations with a nonhorizontal branch (i.e., branch angle $> 15^\circ$ with the ground plane), the branch often split between two sections resulting in commission errors.

In this article, we propose an approach that: 1) accurately models 3-D stem without any prior assumption on its approximate geometry; 2) mitigates the effects of shadowing and point-density variance in TLS data in 3-D stem modeling; and 3) accurately localizes branch-knots from TLS data by identifying branch sections proximal to the stem. Experiments were conducted separately on single- and multiscan data of trees belonging to spruce, birch, and pine species, to access the stem modeling and branch-knot localization potential.

The rest of this article is structured as follows. Section II describes the proposed 3-D stem modeling and branch-knot localization approach. The experiment performed and results obtained are illustrated and discussed in Section III. Finally, Section IV concludes this article.

II. Proposed Method

The proposed 3-D stem modeling and branch-knot localization method is designed to work with both single- and multiscan TLS point clouds of individual trees. The method assumes that: 1) the stem is opaque to laser (i.e., no TLS data point exists inside the stem) and 2) data points exist only on and/or away from the

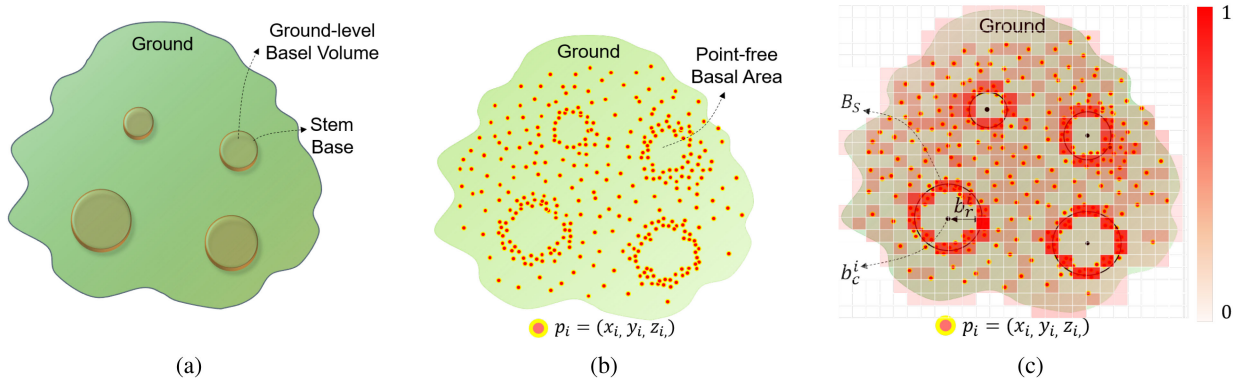

Fig. 2. (a) Forest ground representation shows the span of stem-basal volume (in brown) and the volume free of tree stems (in green). (b) Top view of ground level (i.e., 5 cm above the DEM) TLS data. (c) Corresponding point-density map derived by projecting the ground-level TLS points onto a regular grid of size ζ on the ground plane (i.e., XY plane).

stem surface. Fig. 1 shows the block scheme of the proposed 3-D stem modeling and branch-knot localization approach.

A. Stem Localization and Delineation

The geometry of TLS data collection results in the maximum data point density near the ground and minimum point density near the treetop. Despite a large point-density proximal to the ground, the opacity of stems [see Fig. 2(a)] to laser beam results in circular/near-circular point-free regions at the ground level [see Fig. 2(b)]. We define the ground-level data as the set of all TLS data points at a fixed distance of 5 mm from the digital elevation model (DEM) derived from the TLS point cloud. We use the compound grid and triangulated irregular network (TIN)-based coarse-to-fine iterative method [23] to derive the fine DEM. The specific steps include: 1) dividing the area spanned by the projection of TLS data on the ground plane (i.e., XY plane) into square grids and identifying the lowest point in each grid; 2) generating a TIN model from the points and relative heights of each point from the model; and 3) using the points with the lowest relative height within each grid cell to derive a new TIN model with recalculated relative heights. The coarse and the fine grid sizes were selected by considering the minimum stem size required to be detected and the maximum ground point density in the TLS data, respectively. The near-vertical structure of individual stems will result in a relatively higher ground-level point density at the stem boundary than at the surrounding ground area, where TLS data point density is lower. A normalized point-density grid map of the ground-level data [see Fig. 2(c)] results in point-free regions formed by the opaque stem, which blocks and reflects the laser beams. Thus, the point-free regions take the shape of the stem-basal area, which is nearly circular. We estimate the center $b_c^i, i = [1, Q]$, and the radius $b_r^i, i = [1, Q]$, of the circle B_S that best fits the basal area, for each of Q trees in TLS data using the circular Hough transform [31]. The center of the circle b_c^i is the basal-area center for the ith tree. Let the set of points $T_p = \{p_i \in P\}$, which is within a horizontal distance of $3b_r$ from b_c^i, be associated with a tree [see Fig. 2(c)]. Here, the distance threshold of $3b_r$ is selected under the assumption that: 1) stem is approximately vertical (i.e., $< 15^\circ$ with vertical axis) and 2) stem base region has the largest diameter. The spatial position of every data point in T_p is fully described in the 3-D Euclidean space by x_i, y_i, and z_i coordinates. Let H_t be the z value of the highest point in the individual tree cloud T_p.

B. Voxelization and Subsampling

We divide the volume spanned by the tree point cloud T_p into regular cubical voxels of size ζ to perform subsampling by considering only those data points in T_p that are most proximal to the centroid of the respective voxel. Thus, the point distribution remains very similar to that of the original data [12]. Under the assumption that noisy points in the crown are isolated, we remove all points in voxels with a total point count smaller than a threshold t_v. Voxelization results in $N_v = H_t/\zeta$ divisions along the vertical crown profile. The set of voxels having their respective centroids at the same height is referred in the article as the voxel slice. Let V_X be the set of $N_v - 1$ voxel slices of a tree. It is worth noting that the cubical voxel dimensions are equal; thus, the height of a voxel slice is equal to ζ. Let $W_p \subset T_p$ be the set of points in the subsampled tree point cloud. Fig. 3 shows the representation of voxelized tree crown.

C. Stem Axis Detection

The stem axis refers to the line passing through the set of stem centers in individual voxel slices. We perform the stem axis detection on the subsampled data W_p to minimize the effect of point-density variations along the stem and computational overhead. A single voxel slice often does not contain enough points to estimate the stem center in the slice. Thus, data points in the voxel-slice set $S_G^j = \{[s_j, s_{(j+1)} \ldots s_{(j+f)}]\}$ are used to estimate the stem center location in s_j, where f is the number of proximal upward voxel slices considered. The voxel-slice-set-based stem center estimation is done under the realistic assumption that stem is near vertical in the local vertical crown profile. This voxel-slice-set-based analysis allows us to: 1) increase the number of data points for the stem center location estimation for each voxel slice and 2) mitigate the effect of point-free regions on stem (caused due to laser shadowing by exterior crown sections). In other words, we use all the points in

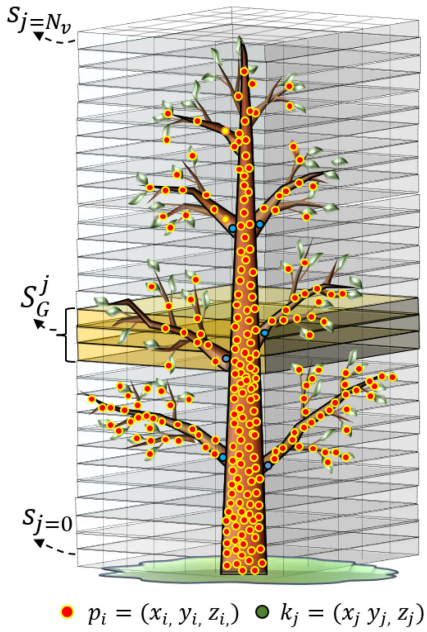

Fig. 3. Cuboidal volume contains the tree stem and the section of branches that grow from the stem. The entire volume is divided into regular voxels of size ζ. The set of voxels that has their centroids at the same height defines a voxel slice s_j. The set of f most proximal voxel slices referred to as the voxel-slice set S_G^j is used in stem-axis modeling.

W_P that are contained by S_G^j to estimate the approximate stem center in the jth voxel slice. We estimate the approximate stem center in the jth voxel slice by: 1) considering all the data points in W_p that fall within the volume spanned by data points in S_G^j; 2) generating a density map based on the point count, where the grid size of the map is set to ζ; 3) performing a circular pattern detection using the circular Hough transform [31] on the 2-D point-density map derived by projecting all the points in S_G^j to the ground plane; and 4) estimating the stem center $c_j = [x_j^c, y_j^c, z_j^c]$ for the jth voxel slice, where $j = [0, N_v]$. Here, x_j^c and y_j^c are the center coordinates of the fitted circle with radius r_c.

The circle defines the approximate cross-sectional shape of the stem section in the S_G^jth voxel slice. The set of stem centers $C = \{c_j\}, j \in [1,\ N_v]$, derived from the individual voxel slices represents the stem axis. It is worth noting that the modeled stem axis passes through the approximate center of the void region in every voxel slice. Hence, the stem axis is used in generating the seed shape required for the down-the-line stem modeling step. Fig. 4 shows the circle of radius r_c fitted on the density map derived from the ground (i.e., XY plane) projected TLS point cloud contained by S_G^j.

D. 3-D Stem Modeling and Branch-Knot Localization

1) 3-D Stem Modeling: We perform stem modeling using T_P (rather than W_P) in order to maximally exploit the structural information present in the TLS data. The stem point set $S \subset T_P$ represents the 3-D stem structure. We model the stem by segmenting the point-free volume inside the stem. The gradient

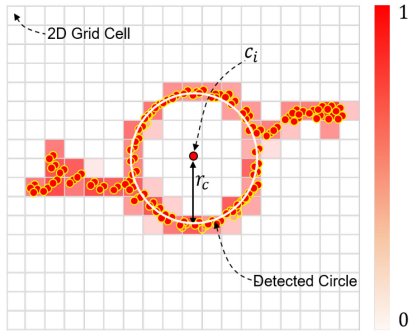

Fig. 4. Normalized 2-D point-density map is derived by projecting TLS data points contained in a voxel-slice set S_G^j, onto a regular grid (with cell size equal to ζ) in the ground (i.e., XY) plane.

vector flow snake (GVF-Snake) 3-D active contour algorithm [32] is used to segment the point-free volume, for its ability to perform an accurate segmentation of the void volume even in the presence of 1) data gaps in the exterior stem surface caused due to laser occlusion/shadowing and 2) surface point-density variability resulting from differences in the sensor perspective and distance to tree components. The objective function to minimize contour energy is given as

$$\int_{\Omega} \sum_{i=1}^{3} (\tau(\Delta v_s^{(i)})^2 + (1-\tau)(((\Delta v_s^{(i)})^2 - 2H(v_s^{(i)})) + U(v_s)dA \rightarrow 0). \quad (1)$$

Here, the void volume to be analyzed be described by the function $f : R^3 \rightarrow R$ and the seed volume $v_s : \Omega \subset R^2 \rightarrow R^3$. The seed volume v_s in our case is a convex hull contained within the void volume of the stem, spanning the entire stem height. We generate the void volume by: 1) placing g uniformly separated seed points at a horizontal distance of h from c_j of the respective voxel slice and 2) generating a convex hull around the superset of all the seed points G from all the voxel slices [see Fig. 5(a)].

Here, $\tau(\Delta v_s^{(i)})^2$ modifies the seed volume such that the total surface area reaches a minimum value and, hence, is referred to as the membrane term. The thin-plate term $(\Delta v_s^{(i)})^2 - 2H(v^{(i)})$ represents the total curvature of the seed volume surface, where $H(v^{(i)})$ is the determinant of the Hessian matrix of $v_{(i)}$. The balancing factor $\tau \in [0,\ 1]$ controls the influence of the membrane and the thin-plate energy terms, i.e., $\tau = 0$ tends to produce a smooth surface with minimum edges, whereas $\tau = 1$ results in a surface that maximally follows the curves on the surface of the stem. The external energy term $O(v_s)$ pulls the points in the seed contours toward the stem boundary defined by the gradient map of the data formed using points in W

$$O(v_s) = -(w_e||\Delta(G_\sigma * f(v_s))|| + w_c f(v_s)) \quad (2)$$

where G_σ denotes a Gaussian kernel with variance σ and Δ is the gradient operator. The coefficients w_e and w_c control the influence of the boundary and the influence of data intensity value, respectively. The problem is solved using the following

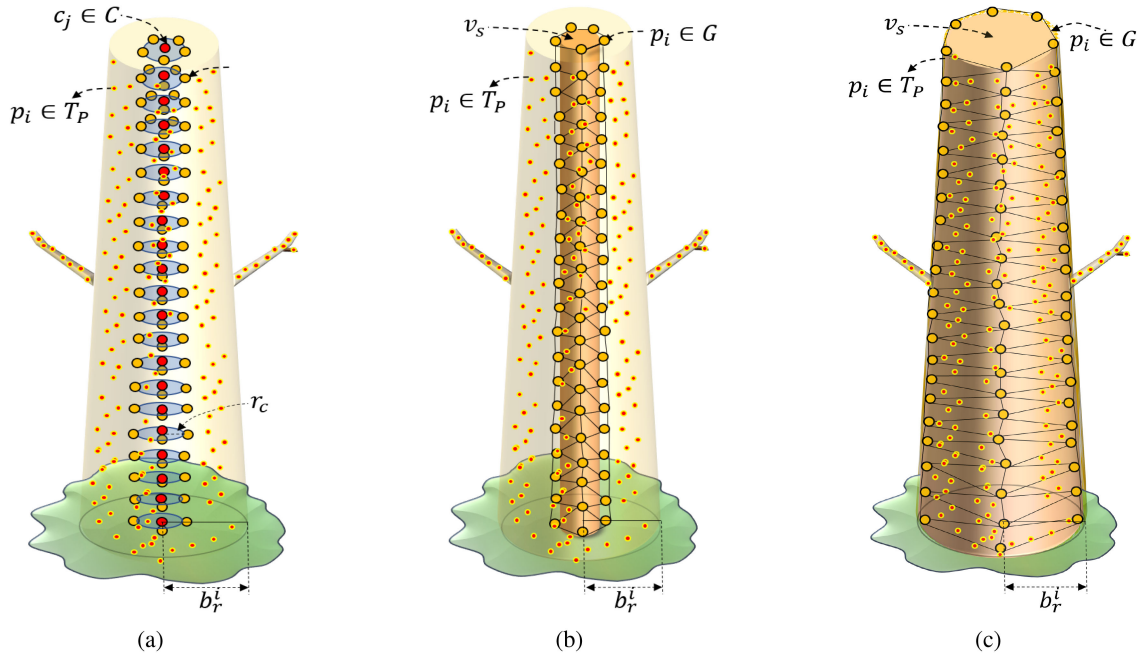

Fig. 5. (a) Stem center c_i (red dots) within each voxel slice is estimated by applying the circular Hough transform to the 2-D point-density map derived by projecting all the points in S_G^j onto the XY plane; the seed point in the set G is placed within the stem volume. (b) Convex hull formed around the seed point set G is provided as the seed volume for the GVF-Snake algorithm. (c) 3-D stem model that spans the void stem volume is obtained by minimizing the GVF-Snake's energy function.

Euler–Lagrange differential equation:

$$\tau \Delta v_s - (1 - v_s)\Delta^2 v_s = \frac{\delta O}{\delta v_s}. \tag{3}$$

The weakly nonlinear differential equation is approximated using the Umbrella function U defined as

$$U(g) := \frac{1}{k} \sum_i (q_i - g) \tag{4}$$

where g is the set of coordinates of the considered vertex, q_i is the set of neighbors in the triangular mesh, and k is the total number of neighbors, i.e., the valence of g. An approximation of Δ^2 is obtained by recursively applying U and estimating the correction c_v. The discrete version of (3) is as follows:

$$(\tau U - (1 - \tau)U^2)(O_k + c_v) = \Delta P \tag{5}$$

where O_k corresponds to the kth row of the system of equations. We can write

$$U(g + c_{v1}) = U(g) - \psi_1 \tag{6}$$

$$U(g + c_{v2}) = U^2(g) - \alpha\psi_2 \tag{7}$$

where $\alpha = 1 + (1/k)\sum(1/k_i)$, with k_i being the valence of the ith neighbor of q_i; the solution to (5) is represented by

$$\psi = \gamma(\tau\psi_1 + 1(1 - \tau)\alpha\psi_2 - \Delta O) \tag{8}$$

where $\psi_1 = U(g)$, $\psi_2 = -\frac{1}{\alpha}(U^2(g))$, and γ is the damping factor that controls the convergence of the iteration procedure.

The energy of the seed volume v_s placed inside the 3-D stem is minimized over a finite number of iterations, by shifting the vertices of the seed volume [see Fig. 5(b)] toward the boundaries of the 3-D stem, forming the 3-D stem model [see Fig. 5(c)]. The 3-D seed volume with minimum energy spans the entire stem void volume and, thus, models the stem without any prior assumptions on the stem geometry. We identify the set of stem points $S_P = \{p_i\} \in W_P$ as the set of data points that falls within a scaled and centered version of the 3-D stem model defined by fitting a convex hull around points in G. We select the scale factor as 0.001 in order to include all the points within 0.001 m (i.e., 1 mm) distance beyond the surface of the 3-D stem model. The typical horizontal cross section of the 3-D stem model at the breast height $\pm\zeta$ that is formed against single- and multiscan TLS data is shown in Fig. 6. It is worth noting that the GVS-Snake's thin-plate energy term in (1) enables the minimization of the total surface area and, hence, prevents the

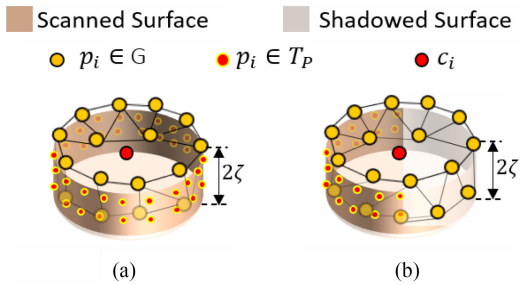

Fig. 6. Stem models for a horizontal stem slice within S_G^j whose stem center is the nearest to the breast height for (a) multiscan TLS data and (b) single-scan TLS data.

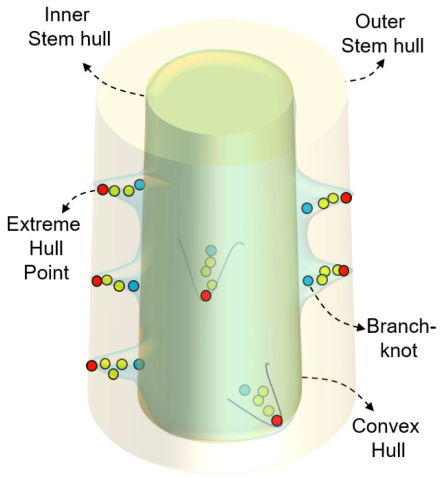

Fig. 7. Points $\in P_{sk}$ are obtained by finding the set difference of points in the inner (green surface) and outer (light-brown surface) hulls fitted on scaled and centered points in G. The vertices of the hull correspond to the extreme points (red dots) in the slice set and are projected onto the stem hull face to derive the location of the branch-knots (blue dots).

model from ballooning-out of the shadowed sections of stem (i.e., sections with no stem points). This forces the stem model to be approximately symmetric around the stem axis even in the absence of points in shadowed sections of the stem. The symmetricity constraint allows us to accurately model the 3-D stem in both single-scan [see Fig. 6(a)] and multiscan [see Fig. 6(b)] data. We estimate stem DBH of a tree as the largest diagonal stem span in the horizontal cross section of the stem model (i.e., the convex hull formed around S) at the breast height.

2) Branch-Knot Localization: The presence of a branch-knot results in locally protruding data points near the modeled stem surface, i.e., the points are found further away from the modeled stem surface. We identify the protruding data points in T_P by: 1) identifying the set of points in $P_{\text{inner}} \in P$ contained by the convex hull scaled along the x- and y-axes, by a factor of 1.001 (i.e., 1-mm increase in hull size); 2) identifying the set of points $P_{\text{outer}} \in P$ that are contained by the convex hull formed around points in G scaled by a factor of 1.05 (i.e., 5-cm increase in hull size); 3) identifying the point set P_{sk} as the set difference of points in P_{outer} and P_{inner}; 4) localizing the extreme points $p_e \in P_{sk}$ by fitting a 3-D convex hull on P_{sk}; and 5) projecting the points onto the nearest triangulated face of original stem hull formed around G, to identify the BKL $K = \{p_k\}, k = [1, K]$. Fig. 7 shows the representation of convex hull fitted on points on a voxel-slice set. The extreme points and their projection on the stem hull/surface are represented as red and blue dots, respectively.

III. Experimental Results

A. Study Area and Dataset Description

Both the single- and multiscan TLS data used in our experiments are from a boreal forest in Evo region located in the south of Finland, with a geographic center point at 61.19°N and 25.11°E. The data were acquired in July 2014 using Leica HDS6100 with a distance measurement accuracy and point spacing of ± 2 and 15.7 mm, respectively, at a distance of 25 m. The beam diameter at exit is 3 mm, with a divergence as low as 2 mrad. The distance measurement accuracy is ≤ 2 mm for solid objects. Single-scan TLS data were acquired by performing the scan from near the center of the plot, and the multiscan TLS data for individual plots were derived by coregistering the data from five single scans conducted at widely separated locations within the plot to minimize occlusions and maximize point density. The data derived from individual single scans were coregistered with the help of reference balls (198.8 mm in diameter) placed in the scan environment. The experiments were conducted on 60 trees located in three 32-by-32 m square plots, which are open data from the international TLS benchmarking project [3]. The trees belong to Scots Pine, Norway Spruce, and Silver Birch. We used the CloudCompare software (version 2.12) to coregister the manually aligned single-scan TLS point clouds for the three square plots. The root-mean-squared coregistration errors (REs) (obtained from the CloudCompare software) associated with the pine, spruce, and birch-dominant plots are 0.6, 1.9, and 1.4 mm, respectively. The basic statistics of the stem DBH for pine, spruce, and birch trees on three plots are shown in Table I. The reference data collected include 1) stem DBH and 2) BKLs. The stem DBH at 1.3 m is recorded as the average of two DBH measurements performed in two perpendicular directions using a steel caliper to the nearest millimeter. The BKLs were derived visually from the point cloud by an expert manual operator using the CloudCompare software. More details of the forest conditions, data, and data acquisition are available in [3].

TABLE I
Specieswise DBH Statistics of the Detected Trees in the Three Square Plots Considered in the Experiments

Tree Species	Number of Trees	Stem DBH (mm)		
		Max	Min	Mean
Pine	20	316.4	183.4	254.3
Spruce	20	422.2	250.2	339.2
Birch	20	334.2	160.6	257.6

B. Experimental Analysis, Results, and Discussion

We evaluate and compare the performance of the proposed stem modeling and branch-knot localization using the following experiments. All the experiments were conducted separately for both the single- and multiscan TLS datasets of the trees belonging to the pine, spruce, and birch species.

1) Assessing the Stem Modeling Performance: Point clouds associated with the individual trees are identified by considering only the stem base circles with radius estimated between 0.1 and 1 m in order to remove spurious stem-basal area centers. Here, the ground points required for the DEM generation are obtained from the TLS data by using the compound grid and TIN-based coarse-to-fine iterative method, by decreasing grid resolution from 0.5 to 0.005 m over successive iterations. The DEM is generated by the inverse distance weighted interpolation on the ground points. The ground-level data are derived as the set of points in the plot-level TLS point cloud within a distance of 5 cm

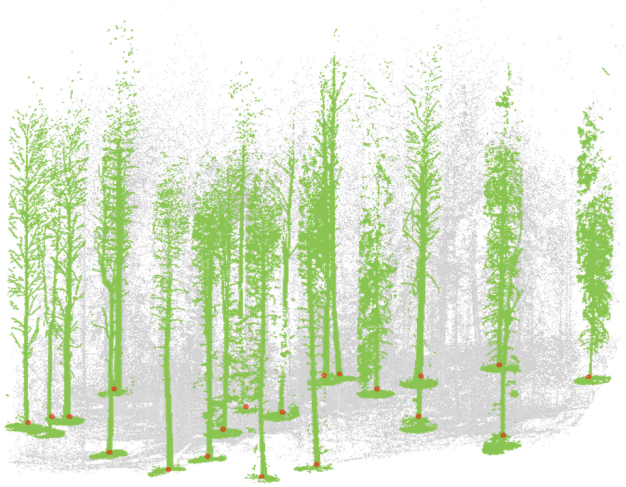

Fig. 8. Point cloud segments (green points) of each tree in a pine-dominant forest plot are delineated by considering all points in the TLS data, which are at a horizontal distance of $3b_r$ from the detected stem-basal center (red dot) in TLS data. The section of point cloud not belonging to the considered trees is shown in gray.

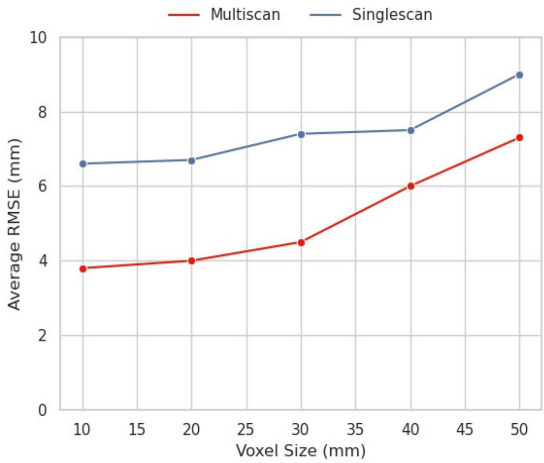

Fig. 9. Average RMSE in stem diameter bias for different voxel sizes.

from the DEM. The point-free circular regions (i.e., basal area of trees) in the XY projected ground-level data are defined by best-fit circles derived using the circular Hough transform [31]. Fig. 8 shows the tree crowns delineated for a pine-dominant plot.

We subsample the tree point cloud T_p by: 1) defining a rectangular volume whose dimensions are derived based on the maximum span of the 3-D point cloud; 2) voxelizing the volume using regular voxels of size ζ; and 3) selecting the points in P that are the most proximal to the centroid of the nonempty voxels. We perform a sensitivity analysis aimed at minimizing the root-mean-squared error (RMSE) associated with DBH estimation bias, by varying ζ from 10 to 50 mm. The optimal ζ value was selected to be 15 mm as it simultaneously minimizes both the DBH estimation error/bias and the computation time (see Fig. 9). We also exclude voxels with less than two data points, as they are very likely to be isolated noisy points resulting from

TABLE II
PARAMETER VALUES USED IN THE EXPERIMENTS

Parameter	Value
Voxel size ζ	0.015 m
Circular Hough Transform sensitivity parameter η_s	0.95
Number of seed point that are uniformly placed around c_j, g	10
Horizontal distance at which the seed points are placed around c_j, h	0.01 m
Number of proximal voxel-slices considered to form S_G, f	4
Convex Hull parameter α_c	0.5
Balancing factor τ	0.5
Damping factor γ	1.0
Number of GVF-Snake iterations N_S	10
Sigma used to calculate the gradient of the image-edge energy σ	2.0
Attraction to edges w_e	2.0
Attraction to lines w_c	0.04

glitches in the electronics. For each delineated tree, all points within the respective horizontal distance $3b_r$ are considered for stem modeling. The stem centers in voxel slices are obtained by applying the circular Hough transform to fit circles on the density map with resolution equal to ζ. The sensitivity parameter η_s of the circular Hough transform is set to 0.95 in order to allow the detection of both partial and complete stem circles and, hence, minimize both the omission and commission errors in stem center detection. A seed volume is placed inside the stem by: 1) generating $g = 10$ points uniformly on the circumference of a circle with radius h and centered at the stem center c_j in the respective voxel slice and 2) fitting a convex hull with $\alpha_c = 0.5$ on the set of all seed points G generated from local stem centers along different tree height slices. The GVF-Snake algorithm is applied with the balancing factor $\tau = 0.5$ to provide equal weights to the membrane energy and the thin-plate energy terms. The damping factor γ is chosen to be 1 to guarantee convergence in the iteration procedure. All the GVF-Snake parameters were selected emphatically to minimize the stem parameter modeling errors (i.e., DBH estimate). The number of iteration N_S was set to 10, as the void stem volume is a smooth point-free region that facilitates the seed volume to reach the stem boundary defined by points in S, with no or minimum hurdle. Fig. 10 shows the initial, intermediate, and final stages of the stem modeling for the [(a)–(c)] multiscan and [(d)–(f)] single-scan data. It can be seen that the model does not expand beyond the point cloud boundary and limits the expansion even in the absence of data points on sections of stem. It is worth noting that the stem model does not balloon-out of small data gaps in multiscan data [see Fig. 10(a)–(c)] or even larger gaps (e.g., when half of the stem surface area is occluded) in single-scan data [see Fig. 10(d)–(f)], which proves the approach to be robust to occlusions. Table II shows the list of all the parameters used in the proposed modeling approach. Fig. 11 shows the stem model of pine [see Fig. 11(a) and (d)], spruce [i.e., Fig. 11(b) and (e)], and birch [i.e., Fig. 11(c) and (f)] obtained using the proposed model with the multiscan and single-scan data, respectively.

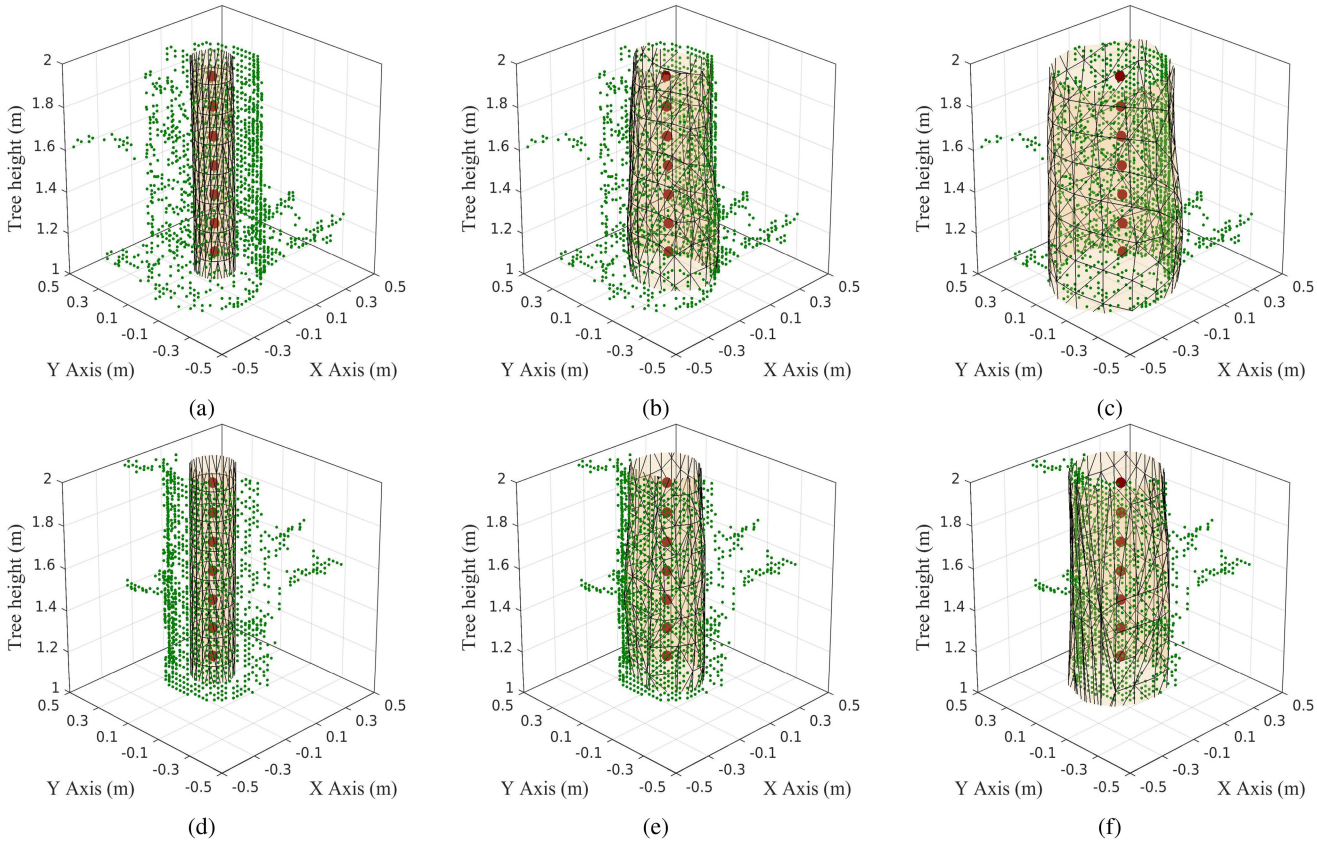

Fig. 10. Geometry of the stem is modeled using the GVF-Snake-based volume segmentation algorithm with seed volume defined by the convex hull formed around G. The GVF-Snake expands the seed volume till the boundary defined by the points in W_p. The initial, intermediate, and final shapes of the seed volume for a section of the tree in the [(a)–(c)] multiscan and [(d)–(f)] single-scan data are shown. The 3-D stem model that spans the void stem volume is obtained by minimizing the GVF-Snake's energy function.

The stem points S are detected by: 1) scaling and centering points in G where the horizontal coordinates (x and y) are scaled by a factor 1.001 (i.e., 1 mm further toward the exterior of the stem surface) and 2) identifying the stem point set S that is the set of all the points in T_P that fall within the convex hull formed around the scaled points. The 1-mm scaling is required as the GVF-Snake algorithm does not expand the volume beyond the stem points. For the multiscan data, the average of the maximum spans of the stem point cloud of a tree in two mutually perpendicular directions at 1.3 m is estimated as the stem DBH. For the single-scan data, the stem DBH is estimated as the maximum span of the stem point cloud at 1.3 m. Fig. 12 shows the point cloud associated with stem of pine [see Fig. 12(a) and (d)], spruce [i.e., Fig. 12(b) and (e)], and birch [i.e., Fig. 12(c) and (f)] obtained using the proposed model using multiscan and single-scan data, respectively. It can be seen that the stem models build on the multiscan data accurately fit the stem geometry for all the three tree species. However, the models tend to expand/bulge-out more in the occluded sections of the single-scan data due to the absence of data points. However, this model bulge at occluded stem sections does not affect the accuracy of stem parameter estimates as they are directly estimated from the stem points and not using the stem model.

We compared the estimation results with: 1) a cylinder fitting method (SoA-CYL) [33] as it is well known and is widely used for stem modeling mostly due to its simplicity and 2) a complementary-fitting-procedure-based stem modeling method (SoA-SNOR) [22], which combines multiple state-of-the art modeling techniques. The SoA-CYL is based on the RANSAC [18], which is an iterative algorithm that considers the noisy nature of data and estimates the optimal model for the randomly selected set of data points that belong to the model. Here, cylinders of different radii, each of which randomly selected 100 points as inliers (i.e., points within 2.5 cm from the cylindrical surface), are generated. Valid cylinders are stored, and the one with the highest number of votes is chosen as the best fit. A best-fit cylinders along tree height describe the radius and orientation of the local stem slices, and hence, a series of such best-fit cylinders obtained from different height slices jointly form the stem model [see Fig. 13(b)]. The SoA-SNOR performs stem modeling by: 1) identifying the subset of TLS data point of tree between 0- and 10-m height, where the occlusion/shadowing effects on the stem are minimal due to the TLS acquisition geometry [20], [22]; 2) dividing the TLS data subset into small patches with maximum diameter of 10 cm; 3) calculating the patch surface normal to determine its orientation with respect to the ground plane (i.e., XY plane) [see Fig. 13(c)]; 4) fitting a cylinder to the set of proximal patches at every 1-m vertical height intervals under the assumption that the normal associated with a stem patch is near parallel ($\leq 15\,^{\circ}$) to the ground plane; 5)

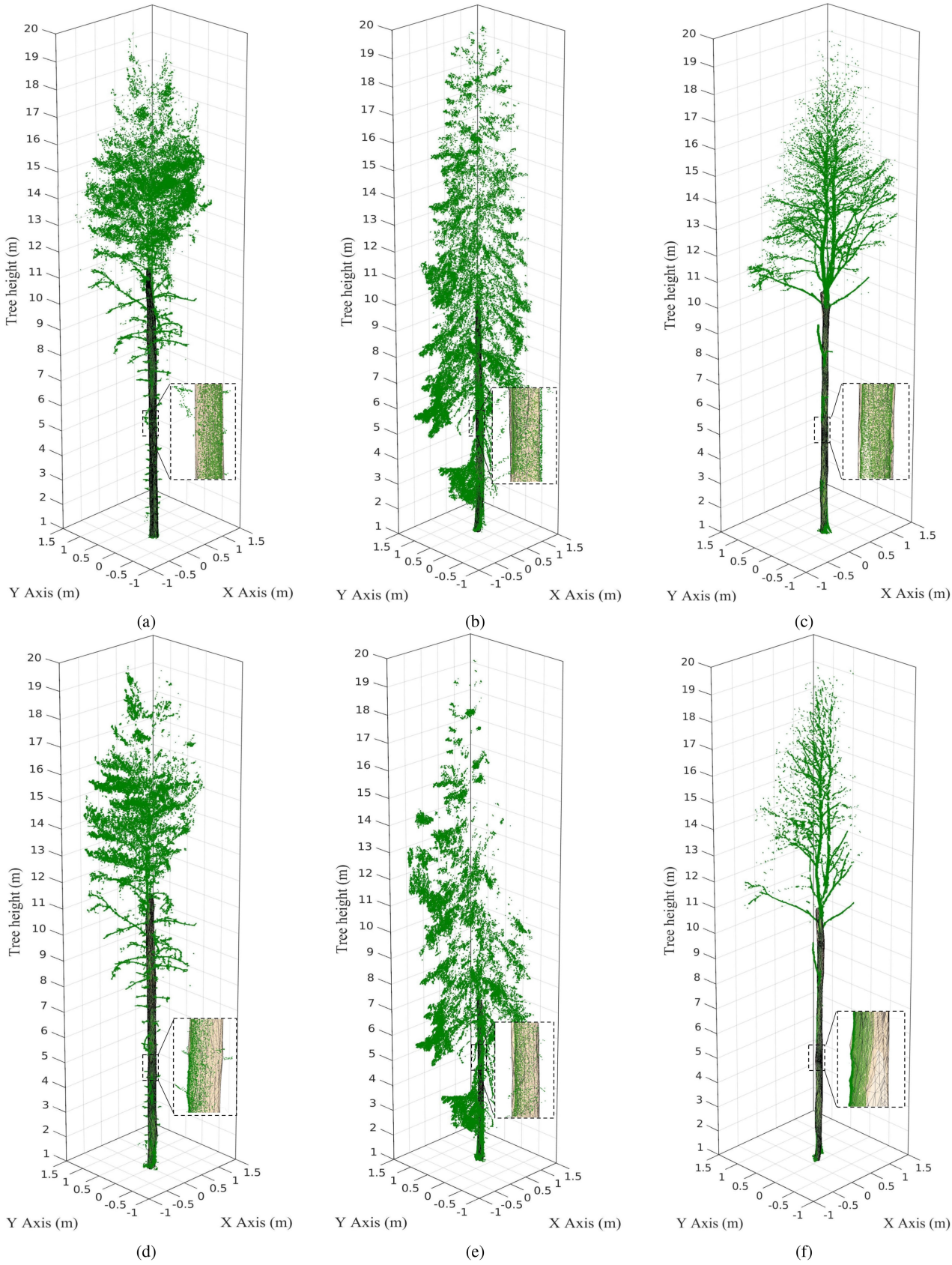

Fig. 11. Stem models derived using the proposed stem modeling approach with multiscan and single-scan TLS data of [(a) and (d)] pine, [(b) and (e)] spruce, and [(c) and (f)] birch tree.

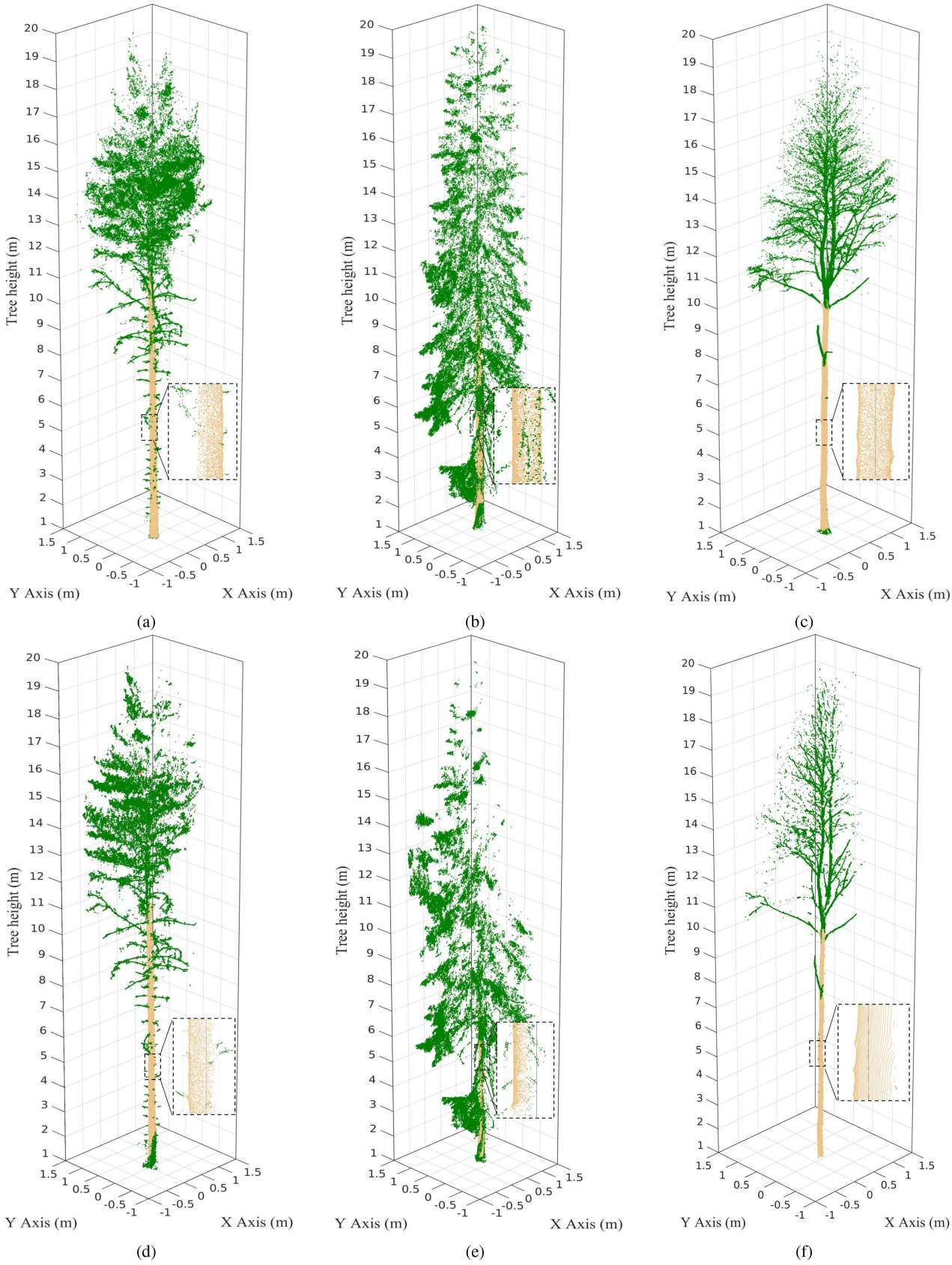

Fig. 12. Stem points (light brown points) derived using the proposed stem modeling approach with multiscan and single-scan TLS data of [(a) and (d)] pine, [(b) and (e)] spruce, and [(c) and (f] birch tree.

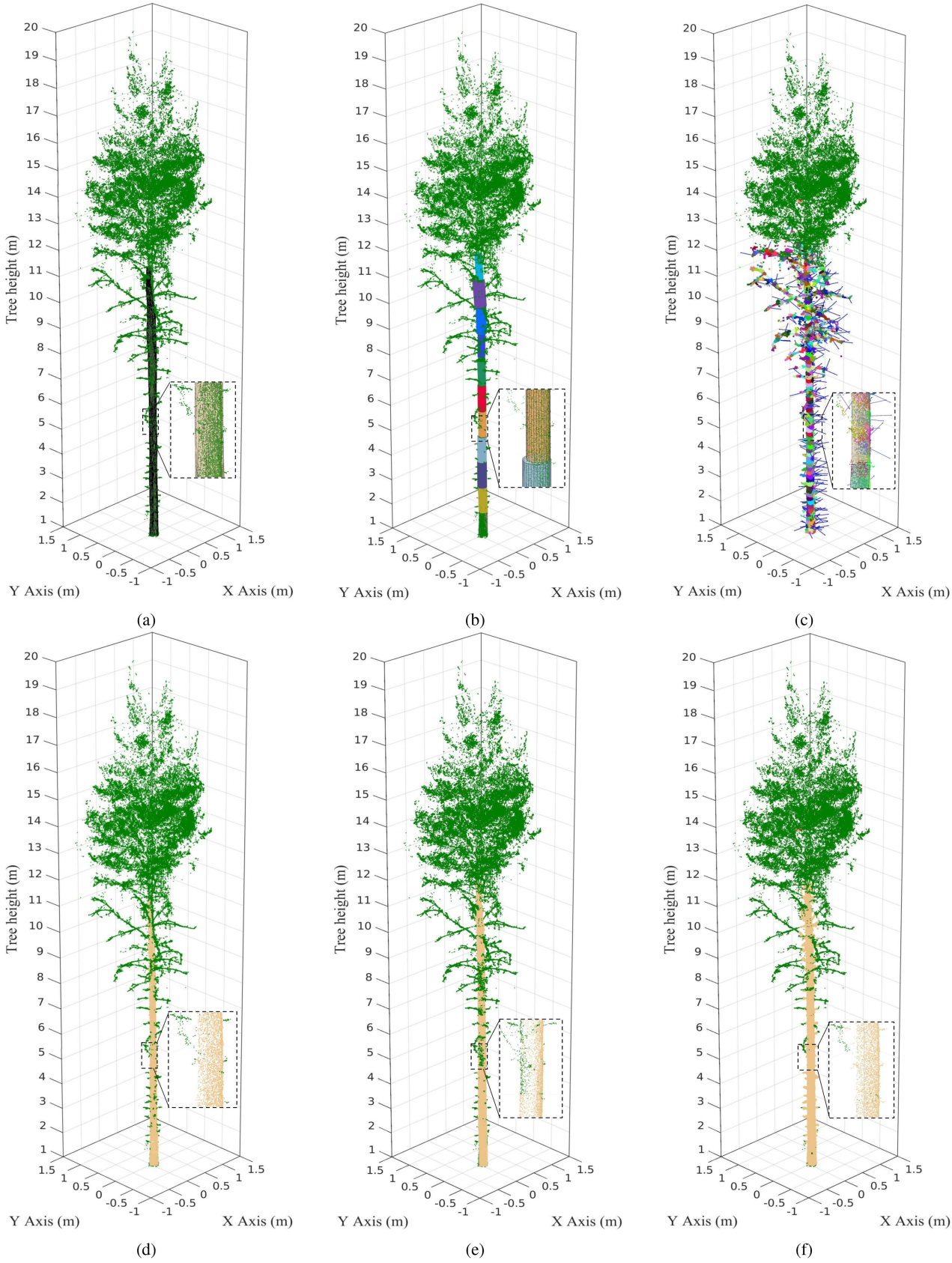

Fig. 13. Stem models and stem points (light brown dots) corresponding to a sample pine, for the [(a) and (d)] proposed, [(b) and (e)] cylinder-fitting-based, and [(c) and (f)] surface-patch normal methods.

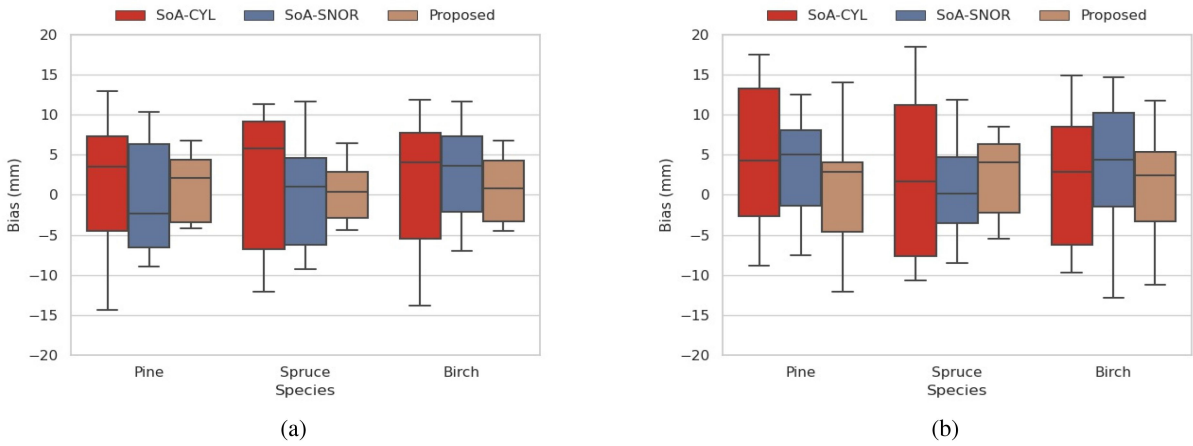

Fig. 14. Boxplot representation of DBH estimation errors obtained for the SoA-CYl, SoA-SNOR, and the proposed method for (a) multiscan and (b) single-scan TLS data.

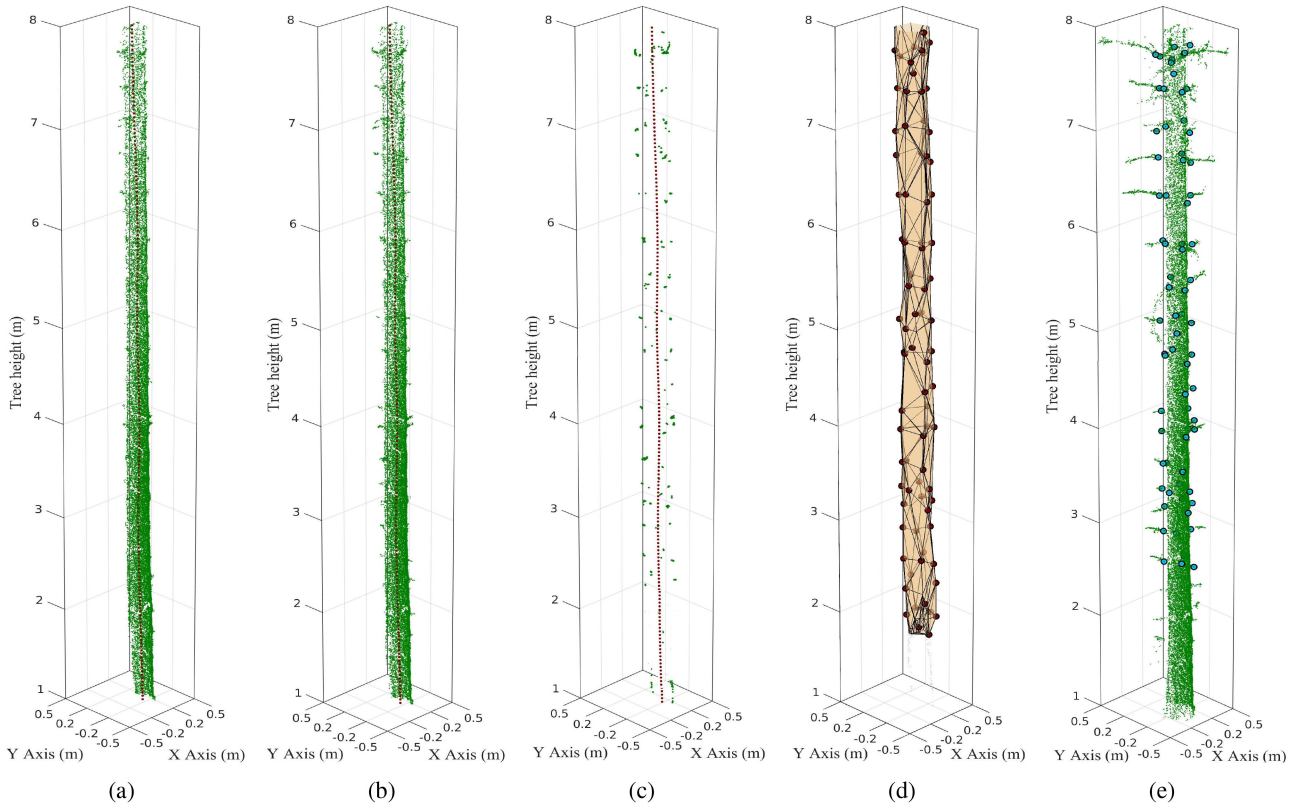

Fig. 15. TLS point cloud contained within the (a) inner and (b) outer hulls represents the stem and the stem with branch sections, respectively. The branch-section point set (c) is identified by performing the set-difference operation between set (a) and (b). The vertices of the convex hull (d) formed on the branch-section point set are shown as red dots. The BKLs (blue dots) are derived by projecting the extreme points (red dots) on to stem surface.

dividing the cylinders further into fine (5 cm) horizontal slice; and 6) estimating the stem diameters in each slice based on circular shape fitting. Tables III and IV show the average DBH estimation errors associated with pine, spruce, and birch trees for the proposed, the SoA-CYL, and the SoA-SNOR approaches, in the case of multiscan and single-scan data, respectively. A qualitative analysis of the three approaches can be done by looking at Fig. 13. It can be clearly seen that the stem points (brown) detected by the proposed approach are more accurate when compared to those obtained using the SoA-CYL and the SoA-SNOR approaches. The boxplot representation of DBH estimation errors obtained for the SoA-BKL and the proposed-BKL method for multiscan and single-scan TLS data are reported in Fig. 14

TABLE III
MEAN ERROR (ME), MEAN ABSOLUTE ERROR (MAE), AND ROOT-MEAN-SQUARED DBH ESTIMATION ERROR (RMSE) FOR MULTISCAN TLS DATA OF PINE, SPRUCE, AND BIRCH SPECIES

Singlescan DBH Estimation Error (mm)									
Species	**Proposed**			**SoA-CYL**			**SoA-SNOR**		
	ME	**MAE**	**RMSE**	**ME**	**MAE**	**RMSE**	**ME**	**MAE**	**RMSE**
Pine	2.5	5.0	5.4	2.0	9.4	10.3	1.6	5.3	6.5
Spruce	2.0	6.7	8.0	5.0	9.3	10.7	3.8	6.3	7.2
Birch	0.7	5.5	6.5	2.2	7.1	8.1	3.4	7.5	8.8

TABLE IV
MEAN ERROR (ME), MEAN ABSOLUTE ERROR (MAE), AND ROOT-MEAN-SQUARED DBH ESTIMATION ERROR (RMSE) FOR SINGLE-SCAN TLS DATA OF PINE, SPRUCE, AND BIRCH SPECIES

Multiscan DBH Estimation Error (mm)									
Species	**Proposed**			**SoA-CYL**			**SoA-SNOR**		
	ME	**MAE**	**RMSE**	**ME**	**MAE**	**RMSE**	**ME**	**MAE**	**RMSE**
Pine	0.3	3.0	3.5	1.8	8.3	8.6	0.6	6.2	7.0
Spruce	1.3	3.8	4.1	1.5	7.0	7.9	0.8	5.7	6.3
Birch	0.8	3.2	3.8	1.8	7.0	7.6	2.4	5.4	6.2

In general, the DBH estimation errors are larger in the single-scan data compared to the multiscan ones. This higher average DBH error in single-scan data is a result of relatively large laser shadowing with respect to the multiscan counterpart. This is in alignment with the finding in other state-of-the-art papers [3]. Fig. 15(a) and (b) shows the boxplot representation of DBH estimation errors obtained for the SoA and the proposed method for the multiscan TLS and single-scan TLS data, respectively. One can clearly see that the proposed method is able to estimate the stem DBH with a minimal error for both single- and multiscan TLS data. The average DBH estimation errors of 3.9 and 6.6 mm for multiscan and single-scan data, respectively, is a quantitative proof of the robustness of the proposed method to the shadowing and point-density variance in the TLS data. For both multiscan and single-scan data, the higher RMSE in DBH bias for the spruce is attributed to the relatively dense branch structure and foliage, compared to pine and birch, which has less stem occlusions.

It is a fact that REs cause deformations in the multiscan point cloud fragments including those corresponding to the stem. Let us now quantify the effect of REs on stem modeling performance. We achieve this by: 1) dividing the trees belonging to each species into three root-mean-squared coregistration error RE_{RMSE} classes, which are the low-RE (0.0 mm $>$ RE_{RMSE} $\leq$ 1.0 mm), the medium-RE (1.0 mm $<$ RE_{RMSE} $\leq$ 1.5 mm), and the high-RE (RE_{RMSE} $>$ 1.5 mm), and 2) quantifying the DBH estimation error for trees in each class. Table V shows the specieswise average DBH estimation error associated with the three RE_{RMSE} classes. The higher RE_{RMSE} in DBH estimates associated with the medium-RE and the high-RE classes compared to the high-RE class reflects the higher amount of stem deformations resulting from REs.

Let us now analyze the impact of the percentage of shadowed stem area S_s on the stem modeling performance. We approximately estimate S_s by dividing the total number of voxels intersected by the stem model to the total number of voxels containing at least one stem point. To quantify the impact of shadowing on stem modeling performance: 1) we divide the trees in the dataset into three classes, which include the low-SH ($25\% < S_s \leq 50\%$), the medium-SH ($50\% < S_s \leq 75\%$), and the high-SH ($S_s > 75\%$) stem shadow class, for each species, and 2) estimate the mean error in DBH estimates for each class. Table VI shows the average DBH estimation error associated with the three stem shadow classes for the three species. It is evident from the DBH estimation errors that the stem shadowing results in stem modeling errors, and the highest DBH estimation errors are associated with the high-SH class. It is also worth noting that the maximum increase in average

TABLE V
DBH ESTIMATION ERRORS FOR THE PINE, BIRCH, AND SPRUCE SPECIES WITH DIFFERENT LEVELS OF COREGISTRATION RMSE FOR THE MULTISCAN TLS DATA

Tree Species	**Coregistration RMSE-Class**	**DBH Estimation Error (mm)**		
		Proposed	**SoA-CYL**	**SoA-SNOR**
Pine	Low-RE	2.9	7.2	6.1
	Medium-RE	3.4	7.8	6.6
	High-RE	3.5	8.4	7.0
Spruce	Low-RE	3.6	6.3	5.5
	Medium-RE	3.1	6.5	5.8
	High-RE	4.2	7.5	6.4
Birch	Low-RE	3.0	6.1	5.4
	Medium-RE	3.5	6.4	6.0
	High-RE	3.8	7.6	6.2

TABLE VI
DBH ESTIMATION ERRORS FOR THE PINE, BIRCH, AND SPRUCE SPECIES WITH DIFFERENT LEVELS OF SHADOWED-STEM-AREA PERCENTAGE FOR THE MULTISCAN TLS DATA

Tree Species	**Stem-Shadow Class**	**DBH Estimation Error (mm)**		
		Proposed	**SoA-CYL**	**SoA-SNOR**
Pine	Low-SH	3.7	7.4	6.8
	Medium-SH	3.9	8.1	7.2
	High-SH	4.1	8.2	7.8
Spruce	Low-SH	4.6	6.9	6.1
	Medium-SH	4.2	7.1	6.5
	High-SH	5.1	7.8	7.3
Birch	Low-SH	4.9	7.1	6.4
	Medium-SH	5.4	8.2	7.2
	High-SH	5.5	7.5	7.4

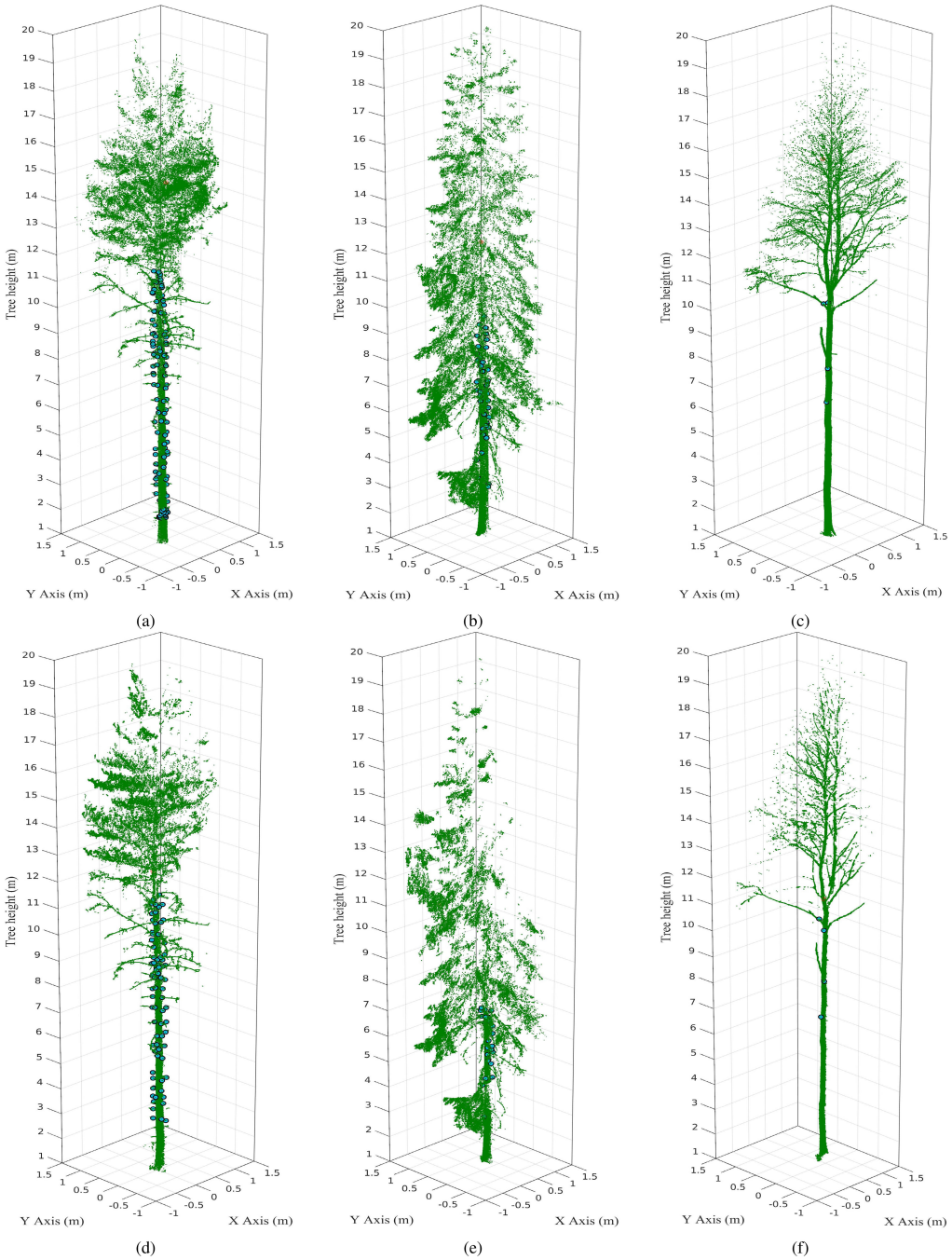

Fig. 16. BKLs (light blue points) derived using the proposed BKL modeling approach with multiscan and single-scan TLS data of [(a) and (d)] pine, [(b) and (e)] spruce, and [(c) and (f)] birch trees.

TABLE VII
MEAN ERROR (ME), MEAN ABSOLUTE ERROR (MAE), AND ROOT-MEAN-SQUARED BRANCH-KNOT LOCALIZATION ERROR (RMSE) FOR MULTISCAN TLS DATA OF PINE, SPRUCE, AND BIRCH SPECIES

Species	Multiscan BKL Localization Error (mm)					
	Proposed-BKL			SoA-BKL		
	ME	MAE	RMSE	ME	MAE	RMSE
Pine	29.6	29.5	29.9	39.5	39.5	39.7
Spruce	36.0	36.0	36.2	50.9	50.9	51.2
Birch	26.5	26.5	26.9	31.2	31.2	31.5

TABLE VIII
MEAN ERROR (ME), MEAN ABSOLUTE ERROR (MAE), AND ROOT-MEAN-SQUARED BKL LOCALIZATION ERROR (RMSE) FOR SINGLE-SCAN TLS DATA OF PINE, SPRUCE, AND BIRCH SPECIES

Species	Singlescan BKL Localization Error (mm)					
	Proposed-BKL			SoA-BKL		
	ME	MAE	RMSE	ME	MAE	RMSE
Pine	28.3	28.3	28.4	40.9	40.9	41.1
Spruce	50.1	50.1	50.3	67.8	67.8	68.0
Birch	42.7	42.7	42.9	49.0	49.0	49.3

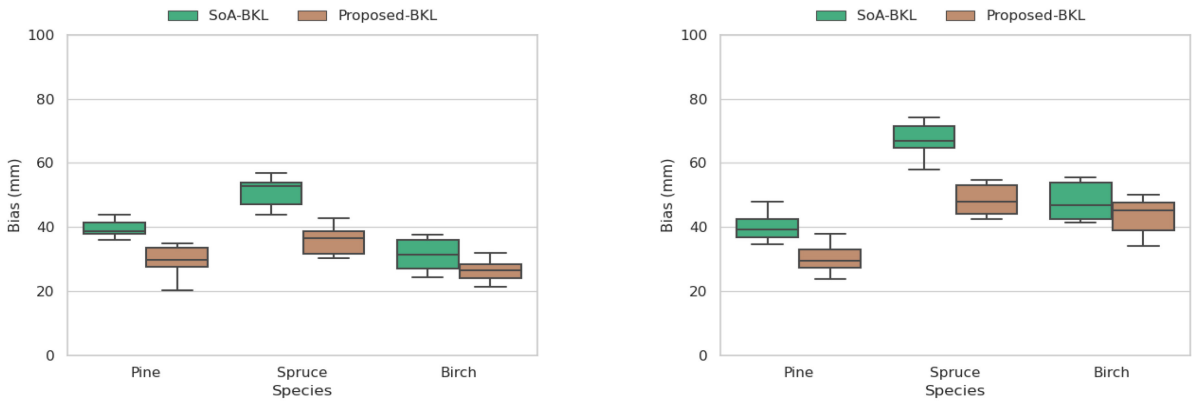

Fig. 17. Boxplot representation of BKL estimation errors obtained for the SoA-BKL and the proposed-BKL method for (a) multiscan and (b) single-scan TLS data.

TABLE IX
PROPORTION OF OMISSION ERROR (OE) AND COMMISSION ERROR (CE) COMPARED TO MANUALLY DETECTED BRANCHES FOR THE PROPOSED-BKL AND THE SOA-BKL APPROACHES, IN THE CASE OF PINE, SPRUCE, AND BIRCH SPECIES

Species	Proposed-BKL				SoA-BKL			
	Multiscan		Singlescan		Multiscan		Singlescan	
	OE	CE	OE	CE	OE	CE	OE	CE
Pine	6.5	5.8	8.8	7.6	8.8	9.5	12.4	14.5
Spruce	9.6	7.4	12.2	11.7	12.4	17.3	21.8	14.3
Birch	7.2	6.8	10.3	9.1	14.4	15.7	17.5	12.3

DBH estimation error is as low as 0.6 mm for the proposed method. However, the maximum increase in DBH estimation errors is 0.9 and 1.2 mm for the SoA-CYL and the SoA-SNOR, respectively.

2) Assessing the Branch-Knot Localization Performance: Branch-knots B_T are detected by: 1) scaling the horizontal (i.e., x and y) components of the data points in G by a factor of 1.01 (i.e., 1 cm further toward the exterior of the stem surface) followed by recentering the scaled points to create a convex hull that includes all the stem points $S \in T_P$ [see Fig. 16(a)]; 2) scaling the horizontal (i.e., x and y) components of the data points in G by a factor of 1.05 (i.e., 5 cm further towards the exterior of the stem surface) followed by recentering the scaled points to create a convex hull that includes all points in T_P that represent both the stem and branch–stem junctions [see Fig. 16(b)]; 3) the detecting extreme points $p_e \in P_{sk}$ by fitting a convex hull with $\alpha = 0.5$ to generate a tight hull-fit while avoiding detection of any inner branch edges and vertices of the point cloud in p_{sk} [see Fig. 16(d)]; and 4) projecting the p_e to the stem surface represented by the hull formed around G [see Fig. 16(e)]. The accuracy of BKL estimates is evaluated by calculating the difference between the estimated and the reference BKLs. Tables VII and VIII show the average branch-knot localization errors associated with pine, spruce, and birch trees for the proposed-BKL and the SoA-BKL approaches in the case of multiscan and single-scan data, respectively. In general, as expected, the branch-knot accuracy is found to be lower for single-scan data due to the relatively lower point density. The boxplot representation of BKL estimation errors obtained for the SoA-BKL and the proposed-BKL method for multiscan and single-scan TLS data are reported in Fig. 17. One can clearly see from the boxplot [see Fig. 17] that the proposed-BKL method is able to more accurately estimate the BKLs by minimizing the localization errors for both single- and multiscan TLS data. In any case, the proposed-BKL method achieve accurate branch-knot localization by accurately detecting stem–branch intersections by avoiding twigs and leaf points, which are often misdetected as branch–stem junctions by the SoA-BKL. In addition, the analysis in the proposed proposed-BKL method is done on the entire stem height rather than on the horizontal stem section, hence avoiding any commission errors caused by tilted branches. The proportions of the omission error (OE) and the commission error (CE) compared to the number of manually detected branches for the proposed-BKL method and the SoA-BKL method for pine, spruce, and birch are shown in Table IX. For the multiscan data, the proposed-BKL approach reduced the OE and the CE proportions by 4.1 and 7.5, respectively, compared to the OE and the CE proportions obtained for the SoA-BKL approach. The reduced errors associated with the proposed-BKL approach is due to the inside-out stem modeling strategy, which is least affected by noisy points outside the stem surface. For the single-scan data, the proportions of the OE and CE were reduced by 6.8 and 4.2, respectively, compared to the SoA-BKL approach. Fig. 17 shows the branch-knots associated with stem of pine [see Fig. 17(a) and (d)], spruce [i.e., Fig. 17(b) and (e)], and birch [i.e., Fig. 17(c) and (f)] obtained using the proposed-BKL model with multiscan and single-scan TLS data, respectively.

IV. Conclusion

A method for accurate 3-D modeling and branch-knot localization in TLS data was proposed. Individual trees were detected and delineated from TLS data by modeling the point-free circular regions formed on the ground due to laser shadowing. The 3-D stem modeling performed by segmenting the void/point-free volume formed inside the stem allowed to accurately capture the stem geometry without any prior assumptions on the geometry. The delineated trees belonged to spruce, pine, and birch species. Unlike the state-of-the-art modeling methods, the proposed inside-out stem modeling method allowed to avoid shadowing errors induced by the proximal branch sections and leaves and also point-density variation. The proposed stem modeling method provided the lowest average RMSE errors in DBH estimates of 3.9 and 6.6 mm, respectively, for the single- and multiscan data. In addition, the increase in DBH estimation error due to improper point cloud coregistration and the increase in the shadowed-stem area is proved to have little effect on the proposed method compared to the state-of-the-art methods. In the case of the proposed-BKL approach, the overall error proportions associated with branch-knot detection decreased by 11.3 and 11.6, respectively, for single- and multiscan data, compared to the error proportions corresponding to the SoA-BKL method. The average branch-knot localization error also reduced by 12.0 and 9.5 mm for the single- and multiscan data, respectively, compared to the BKL error associated with the SoA-BKL method. The proposed stem modeling and branch-knot localization method improved DBH estimation and branch-knot localization performance, respectively, for both multiscan and single-scan TLS data. Future works include evaluating the performance of the method on other tree species with more complex stem structure and canopy.

References

[1] L. Eysn, N. Pfeifer, C. Ressl, M. Hollaus, A. Grafl, and F. Morsdorf, "A practical approach for extracting tree models in forest environments based on equirectangular projections of terrestrial laser scans," *Remote Sens.*, vol. 5, no. 11, pp. 5424–5448, 2013.

[2] P. Raumonen *et al.*, "Fast automatic precision tree models from terrestrial laser scanner data," *Remote Sens.*, vol. 5, no. 2, pp. 491–520, 2013.

[3] X. Liang *et al.*, "International benchmarking of terrestrial laser scanning approaches for forest inventories," *ISPRS J. Photogramm. Remote Sens.*, vol. 144, pp. 137–179, 2018.

[4] X. Liang *et al.*, "Terrestrial laser scanning in forest inventories," *ISPRS J. Photogramm. Remote Sens.*, vol. 115, pp. 63–77, 2016.

[5] M. Simonse, T. Aschoff, H. Spiecker, and M. Thies, "Automatic determination of forest inventory parameters using terrestrial laser scanning," in *Proc. Scandlaser Sci. Workshop Airborne Laser Scanning Forests*, 2003, pp. 252–258.

[6] X. Liang, V. Kankare, X. Yu, J. Hyyppa, and M. Holopainen, "Automated stem curve measurement using terrestrial laser scanning," *IEEE Trans. Geosci. Remote Sens.*, vol. 52, no. 3, pp. 1739–1748, Mar. 2014.

[7] M. Hauglin, R. Astrup, T. Gobakken, and E. Næsset, "Estimating single-tree branch biomass of Norway spruce with terrestrial laser scanning using voxel-based and crown dimension features," *Scand. J. Forest Res.*, vol. 28, no. 5, pp. 456–469, 2013.

[8] X. Liang, P. Litkey, J. Hyyppa, H. Kaartinen, M. Vastaranta, and M. Holopainen, "Automatic stem mapping using single-scan terrestrial laser scanning," *IEEE Trans. Geosci. Remote Sens.*, vol. 50, no. 2, pp. 661–670, Feb. 2012.

[9] E. Lindberg, J. Holmgren, K. Olofsson, and H. Olsson, "Estimation of stem attributes using a combination of terrestrial and airborne laser scanning," *Eur. J. Forest Res.*, vol. 131, no. 6, pp. 1917–1931, 2012.

[10] G. Brolly and G. Kiraly, "Algorithms for stem mapping by means of terrestrial laser scanning," *Acta Silvatica et Lignaria Hungarica*, vol. 5, pp. 119–130, 2009.

[11] K. Olofsson, J. Holmgren, and H. Olsson, "Tree stem and height measurements using terrestrial laser scanning and the RANSAC algorithm," *Remote Sens.*, vol. 6, no. 5, pp. 4323–4344, 2014.

[12] A. Harikumar, F. Bovolo, and L. Xinlian, "An effective approach to 3D stem modeling and branch-knot localization in multiscan TLS data," in *Proc. IEEE Int. Geosci. Remote Sens. Symp.*, 2019, pp. 6075–6078.

[13] M. Thies*, N. Pfeifer, D. Winterhalder, and B. G. Gorte, "Three-dimensional reconstruction of stems for assessment of taper, sweep and lean based on laser scanning of standing trees," *Scand. J. Forest Res.*, vol. 19, no. 6, pp. 571–581, 2004.

[14] W. Gander, R. Strebel, and G. H. Golub, "Fitting of circles and ellipses least squares solution," in *SVD and Signal Processing III, Algorithms, Architectures and Applications*. Amsterdam, The Netherlands: Elsevier, 1995, pp. 349–356.

[15] J. G. Henning and P. J. Radtke, "Detailed stem measurements of standing trees from ground-based scanning lidar," *Forest Sci.*, vol. 52, no. 1, pp. 67–80, 2006.

[16] G. Bu and P. Wang, "Adaptive circle-ellipse fitting method for estimating tree diameter based on single terrestrial laser scanning," *J. Appl. Remote Sens.*, vol. 10, no. 2, 2016, Art. no. 026040.

[17] A. Nurunnabi, Y. Sadahiro, R. Lindenbergh, and D. Belton, "Robust cylinder fitting in laser scanning point cloud data," *Measurement*, vol. 138, pp. 632–651, 2019.

[18] M. A. Fischler and R. C. Bolles, "Random sample consensus: A paradigm for model fitting with applications to image analysis and automated cartography," *Commun. ACM*, vol. 24, no. 6, pp. 381–395, 1981.

[19] J. Holmgren, M. Tulldahl, J. Nordlöf, E. Willén, and H. Olsson, "Mobile laser scanning for estimating tree stem diameter using segmentation and tree spine calibration," *Remote Sens.*, vol. 11, no. 23, 2019, Art. no. 2781.

[20] K. Olofsson and J. Holmgren, "Single tree stem profile detection using terrestrial laser scanner data, flatness saliency features and curvature properties," *Forests*, vol. 7, no. 9, 2016, Art. no. 207.

[21] J. Pyörälä *et al.*, "Assessing branching structure for biomass and wood quality estimation using terrestrial laser scanning point clouds," *Can. J. Remote Sens.*, vol. 44, no. 5, pp. 462–475, 2018.

[22] T. P. Pitkänen, P. Raumonen, and A. Kangas, "Measuring stem diameters with TLS in boreal forests by complementary fitting procedure," *ISPRS J. Photogramm. Remote Sens.*, vol. 147, pp. 294–306, 2019.

[23] G. Király and G. Brolly, "Tree height estimation methods for terrestrial laser scanning in a forest reserve," *Int. Arch. Photogramm., Remote Sens. Spatial Inf. Sci.*, vol. 36, no. 3/W52, pp. 211–215, 2007.

[24] B. Gorte and N. Pfeifer, "Structuring laser-scanned trees using 3d mathematical morphology," *Int. Arch. Photogramm. Remote Sens.*, vol. 35, no. B5, pp. 929–933, 2004.

[25] T. P. Pitkänen, P. Raumonen, X. Liang, M. Lehtomäki, and A. Kangas, "Improving TLS-based stem volume estimates by field measurements," *Comput. Electron. Agriculture*, vol. 180, 2021, Art. no. 105882.

[26] T. Yrttimaa *et al.*, "Multisensorial close-range sensing generates benefits for characterization of managed scots pine (Pinus sylvestris L.) stands," *ISPRS Int. J. Geo-Inf.*, vol. 9, no. 5, 2020, Art. no. 309.

[27] S. Krisanski, M. S. Taskhiri, S. G. Aracil, D. Herries, and P. Turner, "Sensor agnostic semantic segmentation of structurally diverse and complex forest point clouds using deep learning," *Remote Sens.*, vol. 13, no. 8, 2021, Art. no. 1413.

[28] Z.-L. Cheng, X.-P. Zhang, and B.-Q. Chen, "Simple reconstruction of tree branches from a single range image," *J. Comput. Sci. Technol.*, vol. 22, no. 6, pp. 846–858, 2007.

[29] J. Pyörälä *et al.*, "Quantitative assessment of scots pine (Pinus sylvestris L.) whorl structure in a forest environment using terrestrial laser scanning," *IEEE J. Sel. Topics Appl. Earth Observ. Remote Sens.*, vol. 11, no. 10, pp. 3598–3607, Oct. 2018.

[30] J. Pyörälä *et al.*, "Variability of wood properties using airborne and terrestrial laser scanning," *Remote Sens. Environ.*, vol. 235, 2019, Art. no. 111474.

[31] K. Carolyn, D. Ballard, and J. Sklansky, "Finding circles by an array of accumulators," *Commun. ACM*, vol. 18, no. 2, pp. 120–122, 1975.

[32] C. Lürig, L. Kobbelt, and T. Ertl, "Hierarchical solutions for the deformable surface problem in visualization," *Graph. Models*, vol. 62, no. 1, pp. 2–18, 2000.

[33] A. Nurunnabi, Y. Sadahiro, and R. Lindenbergh, "Robust cylinder fitting in three-dimensional point cloud data," *Int. Arch. Photogramm. Remote Sens. Spatial Inf. Sci.*, vol. 42, no. 1/W1, pp. 63–70, 2017.

Aravind Harikumar (Member, IEEE) received the B.Tech. degree in electronics and communication engineering from the University of Kerala, Thiruvananthapuram, India, in 2007, the M.Tech. degree in remote sensing and wireless sensor networks from Amrita Vishwa Vidyapeetham, Coimbatore, India, in 2011, the M.Sc. degree in geoinformatics from the ITC-Faculty of Geo-Information Science and Earth Observation, University of Twente, Enschede, The Netherlands, in 2014, and the Ph.D. degree in information and communication technology from the University of Trento, Trento, Italy, in 2019.

He is currently a Postdoctoral Fellow with the University of Toronto Mississauga, Mississauga, ON, Canada. He studies vegetation dynamics using remote sensing and machine learning techniques. His research interests include tree species/genotype classification and forest parameter estimation using unmanned-aerial-vehicle-based optical and light detection and ranging remote sensing data.

Dr. Harikumar is a reviewer for many international journals including IEEE TRANSACTIONS ON GEOSCIENCE AND REMOTE SENSING, IEEE GEOSCIENCE AND REMOTE SENSING LETTERS, and *ISPRS Journal of Photogrammetry and Remote Sensing*.

Xinlian Liang (Senior Member, IEEE) received his doctoral degree in Geoinformatics from Aalto University, Finland, in 2013.

He is now leading the Multi-Source Perception and Consciousness (M-SPACE) group at Wuhan University (WH). Before WH, he was a Research Manager and the leader of smart forest group at the Department of Remote Sensing and Photogrammetry, Finnish Geospatial Research Institute. His publication list includes 80+ Web-of-Science-listed papers, including 6 ESI hot/highly cited papers. He has been the Associated Editor of Forest Ecosystems since 2018, the Chair of "Thematic Information Extraction" Working Group of the International Society for Photogrammetry and Remote Sensing since 2016, and the Chair/Co-Chair/Area Chair/Track Chair of several international conferences/workshops. His current research interests include innovative automation and geospatial techniques in digitizing and modeling forest ecosystems, with all kinds of point cloud as well as imaging technologies.

Francesca Bovolo (Senior Member, IEEE) received the Laurea (B.S.) and Laurea Specialistica (M.S.) degrees (*summa cum laude*) in telecommunication engineering in 2001 and 2003, respectively, and the Ph.D. degree in communication and information technologies in 2006, all from the University of Trento, Trento, Italy.

She was a Research Fellow with the University of Trento until 2013. She is currently the Founder and the Head of the Remote Sensing for Digital Earth Unit, Fondazione Bruno Kessler, Trento, and a Member of the Remote Sensing Laboratory, Trento. She is one of the co-investigators of the Radar for Icy Moon Exploration instrument of the European Space Agency Jupiter Icy Moons Explorer and a Member of the science study team of the EnVision mission to Venus. She conducts research on her research interests within the context of several national and international projects. Her research interests include remote sensing image processing; multitemporal remote sensing image analysis; change detection in multispectral, hyperspectral, and synthetic aperture radar images and very high resolution images; time-series analysis; content-based time-series retrieval; domain adaptation; light detection and ranging; and radar sounders.

Dr. Bovolo is a member of the program and scientific committee of several international conferences and workshops. She was a recipient of the First Place in the Student Prize Paper Competition of 2006 IEEE International Geoscience and Remote Sensing Symposium in Denver, CO, USA. She was the Technical Chair of the International Workshop on the Analysis of Multitemporal Remote-Sensing Images in 2011 and 2019. She has been a Co-Chair of the SPIE International Conference on Signal and Image Processing for Remote Sensing since 2014. She is the Publication Chair of the International Geoscience and Remote Sensing Symposium in 2015. She has been an Associate Editor for IEEE JOURNAL OF SELECTED TOPICS IN APPLIED EARTH OBSERVATIONS AND REMOTE SENSING since 2011 and a Guest Editor for the Special Issue on Analysis of Multitemporal Remote Sensing Data of IEEE TRANSACTIONS ON GEOSCIENCE AND REMOTE SENSING. She is a referee for several international journals.

Lorenzo Bruzzone (Fellow, IEEE) received the Laurea (M.S.) degree (*summa cum laude*) in electronic engineering and the Ph.D. degree in telecommunications from the University of Genoa, Genoa, Italy, in 1993 and 1998, respectively.

He is currently a Full Professor of Telecommunications with the University of Trento, Trento, Italy, where he teaches remote sensing, radar, and digital communications. He is the Founder and the Director of the Remote Sensing Laboratory, Department of Information Engineering and Computer Science, University of Trento. He is the Principal Investigator of many research projects. He is also the Principal Investigator of the Radar for Icy Moon Exploration instrument in the framework of the Jupiter Icy Moons Explorer mission of the European Space Agency (ESA) and the Science Lead for the High Resolution Land Cover project in the framework of the Climate Change Initiative of ESA. He is the author or co-author of 294 scientific publications in referred international journals (221 in IEEE journals), more than 340 papers in conference proceedings, and 22 book chapters. He is Editor/Co-Editor of 18 books/conference proceedings and one scientific book. His papers are highly cited, as proven from the total number of citations (more than 41 000) and the value of the H-index (93) (source: Google Scholar). He was invited as a Keynote Speaker in more than 40 international conferences and workshops. He promotes and supervises research on his research areas within the frameworks of many national and international projects. His current research interests include remote sensing, radar and synthetic aperture radar, signal processing, machine learning, and pattern recognition.

Dr. Bruzzone has been a member of the Administrative Committee of the IEEE Geoscience and Remote Sensing Society (GRSS) since 2009. He has been a Vice-President for Professional Activities of the IEEE GRSS since 2019. He ranked first place in the Student Prize Paper Competition of the 1998 IEEE International Geoscience and Remote Sensing Symposium (IGARSS), Seattle, WA, USA, July 1998. He was the recipient of many international and national honors and awards, including the recent IEEE GRSS 2015 Outstanding Service Award, the 2017 and 2018 IEEE IGARSS Symposium Prize Paper Awards, and the 2019 WHISPER Outstanding Paper Award. He was a Guest Co-Editor for many special issues of international journals. He is the Co-Founder of the IEEE International Workshop on the Analysis of Multitemporal Remote-Sensing Images series and is a Member of the Permanent Steering Committee of this series of workshops. Since 2003, he has been the Chair of the SPIE Conference on Image and Signal Processing for Remote Sensing. He is the Founder of the *IEEE Geoscience and Remote Sensing Magazine* for which he was the Editor-in-Chief between 2013 and 2017. He is an Associate Editor for IEEE TRANSACTIONS ON GEOSCIENCE AND REMOTE SENSING. He was a Distinguished Speaker of the IEEE Geoscience and Remote Sensing Society between 2012 and 2016.